

ASME Journal of Heat and Mass Transfer Online journal at:

https://asmedigitalcollection.asme.org/heattransfer



Partha Pratim Chakraborty

Alan Levin
Department of Mechanical and Nuclear
Engineering,
Kansas State University,
3002 Rathbone Hall,
1701B Platt Street,
Manhattan, KS 66506
e-mail: parthapratim@ksu.edu

Melanie M. Derby

Mem. ASME
Alan Levin Department of Mechanical and
Nuclear Engineering,
Kansas State University,
3002 Rathbone Hall,
1701B Platt Street,
Manhattan, KS 66506
e-mail: derbym@ksu.edu

Analysis of Drying Front Propagation and Coupled Heat and Mass Transfer During Evaporation From Additively Manufactured Porous Structures Under a Solar Flux

Drying front propagation and coupled heat and mass transfer analysis from porous media is critical for soil—water dynamics, electronics cooling, and evaporative drying. In this study, de-ionized water was evaporated from three 3D printed porous structures (with 0.41 mm, 0.41 mm, and 0.16 mm effective radii, respectively) created out of acrylonitrile butadiene styrene (ABS) plastic using stereolithography technology. The structures were immersed in water until all the pores were invaded and then placed on the top of a sensitive scale to record evaporative mass loss. A 1000 W/m² heat flux was applied with a solar simulator to the top of each structure to accelerate evaporation. The evaporative mass losses were recorded at 15 min time intervals and plotted against time to compare evaporation rates from the three structures. The evaporation phenomena were captured with a high-speed camera from the side of the structures to observe the drying front propagation during evaporation, and a high-resolution thermal camera was used to capture images to visualize the thermal gradients during evaporation. The 3D-structure with the smallest effective pore radius (i.e., 0.16 mm) experienced the sharpest decrease in the mass loss as the water evaporated from 0.8 g to 0.1 g within 180 min. The designed pore structures influenced hydraulic linkages, and therefore, evaporation processes. A coupled heat-and-mass-transfer model modeled constant rate evaporation, and the falling rate period was modeled through the normalized evaporation rate. [DOI: 10.1115/1.4063766]

Keywords: solar, porous media, drying front, heat and mass transfer

1 Introduction and Literature Review

Evaporation from porous media coupled with heat and mass transfer under influence of external heat flux is a complex phenomenon relevant in sectors such as electronics cooling [1–3], heat pipes [4,5], fuel cells [6,7], and conservation of water in soils [8–11]. Different parameters such as pore sizes or porous structure formation [11–13], characteristic length [8,11,14], liquid island formation [15–18], hydraulic connection [17,19–22], and coupled heat/mass transport [6,23–25] influence evaporation rates and mechanisms.

Evaporation from porous media can be categorized into three distinct periods: constant rate, falling rate, and slower rate periods [8–11,14,16,17,26–28]. In a fully saturated porous media, liquid is evaporated from the top surface at a constant rate. The constant rate of evaporation continues while a hydraulic linkage is maintained through the saturated and unsaturated portion by means of capillary

¹Corresponding author.

Contributed by the Heat Transfer Division of ASME for publication in the JOURNAL OF HEAT AND MASS TRANSFER. Manuscript received July 21, 2023; final manuscript received September 25, 2023; published online November 9, 2023. Assoc. Editor: Yun Wang.

action. When this hydraulic linkage breaks down, evaporation experiences a sharp decrease and enters into the falling rate period. The maximum distance between the saturated and unsaturated portion at the end of constant rate period is indicated as the characteristic length, and it plays a vital role in evaporation. The constant rate period elongates for larger characteristic lengths [8,11]. In the falling rate period, the continuous hydraulic linkages break down and small liquid islands are formed between the particles of porous structure, which leads to enhanced vapor diffusion. At the later stage (i.e., slower rate period), the liquid islands start to break up and the evaporation is dominated by diffusion. During the slower rate period, evaporation rate significantly decreases (e.g., 0–1 mm/day) [9,11,26].

Evaporation from porous structures depends primarily on pore sizes and its subsequent effects on capillary action. In the study of Lehmann et al. [11], liquid was transported from interconnected porous structure of larger pores to smaller pores due to capillary action and subsequently created a continuous hydraulic chain through the saturated and unsaturated parts. Nachshon et al. [12] observed an elongated constant rate period (\sim 7 days) in porous media consisting of smaller particles (i.e., 150–300 μ m) compared

to larger particles (i.e., 1-2 mm), as smaller particles create smaller pore sizes. The constant rate period elongated more in a porous matrix of smaller pore sizes than larger pores (i.e., particle sizes ranging from 6 nm to 45 μ m) [13]. The constant rate of evaporation was more dominant with porous structure consisting of mixed pore sizes (i.e., larger and smaller pores) than uniform porous configuration due to higher capillary potential differences [12].

Formation of liquid islands between multiple particles across the porous structure affects evaporation mechanisms [29,30]. Liquid islands across the structure create a continuous hydraulic linkage between saturated and unsaturated portions. In a study of evaporation from heterogeneous sand column (260 mm of height, 75 mm of width, and 11 mm of thickness), liquid islands were formed between adjacent particles, leading to a supply of water to the evaporative surface with continuous liquid chain [9,16,17]. Shokri et al. [17] noted the presence of two evaporative fronts (i.e., primary and secondary), where a liquid connection was maintained between both fronts created with liquid islands. The term "secondary capillary effect" was mentioned by Chen et al. [19,20], where the liquid islands were formed in cylindrical porous structure and created a hydraulic effect toward the evaporative front. For evaporation from 2D-networks (i.e., where the thickness is negligible compared to length and width) [18,31,32], the liquid films contributed significantly to form hydraulic connection leading to a stable evaporation rate.

Evaporation from porous media under the influence of external heat source is a coupled heat/mass transfer phenomenon that has been studied along with the effects of porous structure, capillary action, and evaporation stages [6,15,23–25]. In a fuel cell diffusion media, natural-convection-induced evaporation was experimentally investigated and modeled, along with mass transport consideration [6]. Cho and Mench [6] theoretically and experimentally proved the association of longer constant rate period with formation of liquid islands leading to continuous liquid islands. Chakraborty et al. [15] experimented with porous media consists of similar sized (2.38-mm-diameter) glass and Teflon spheres under influence of a solar-simulated heat flux (i.e., 1000 W/m²). The coupled heat and mass transport were influenced by capillary action and hydraulic linkage during evaporation from hydrophilic and hydrophobic media. Horri

et al. [23] experimented with solar evaporation in light-absorbing porous material (i.e., carbon-Fe $_3$ O $_4$ composite) and the model included contributions of solar irradiance along with natural convection during evaporation; the model matched the experiment within 4.67–13.2%. Zannouni et al. [24] modeled diffusive evaporation numerically along with mass transport, and significant agreement was noticed between theoretical and experimental analysis.

Evaporation from porous media is a coupled heat and mass transfer phenomenon that is influenced by parameters such as pore size, capillary action, hydraulic linkage, liquid islands, and applied heat fluxes. In this study, evaporation was studied from three additively manufactured porous structures. The advantages of using these structures compared to natural porous media (e.g., sand or soil) are the controllable pore sizes and structures due to precision of the manufacturing process (i.e., ±0.1 mm of thickness resolution), compared to natural porous media with structures that vary depending on porosity, bulk density, and other parameters [8]. In this study, the pore sizes were kept constant to reduce variability of complex porous media and the steady-state solution of mass transfer during evaporation was modeled. In addition, in a controllable porous structure, the water movement during evaporation as well as hydraulic linkages can be analyzed properly and these fundamental findings are useful in solving complex transient heat/mass transfer in real porous media with complex microstructures. The main objectives of this study are to (1) analyze evaporation phenomena from three different additively manufactured structures with different pore sizes and understand water transport due to lateral movement restriction, (2) understand and study the effects of pore sizes, capillary actions, and subsequent formation of liquid islands and its effects on different stages of evaporation, (3) formulate steady-state coupled heat and mass transfer model to analyze evaporation under the influence of heat flux, and (4) model transient heat and mass transfer during the falling rate period of evaporation.

2 Experimental Apparatus

In this study, de-ionized water was evaporated from three additively manufactured porous structures. The discussion of

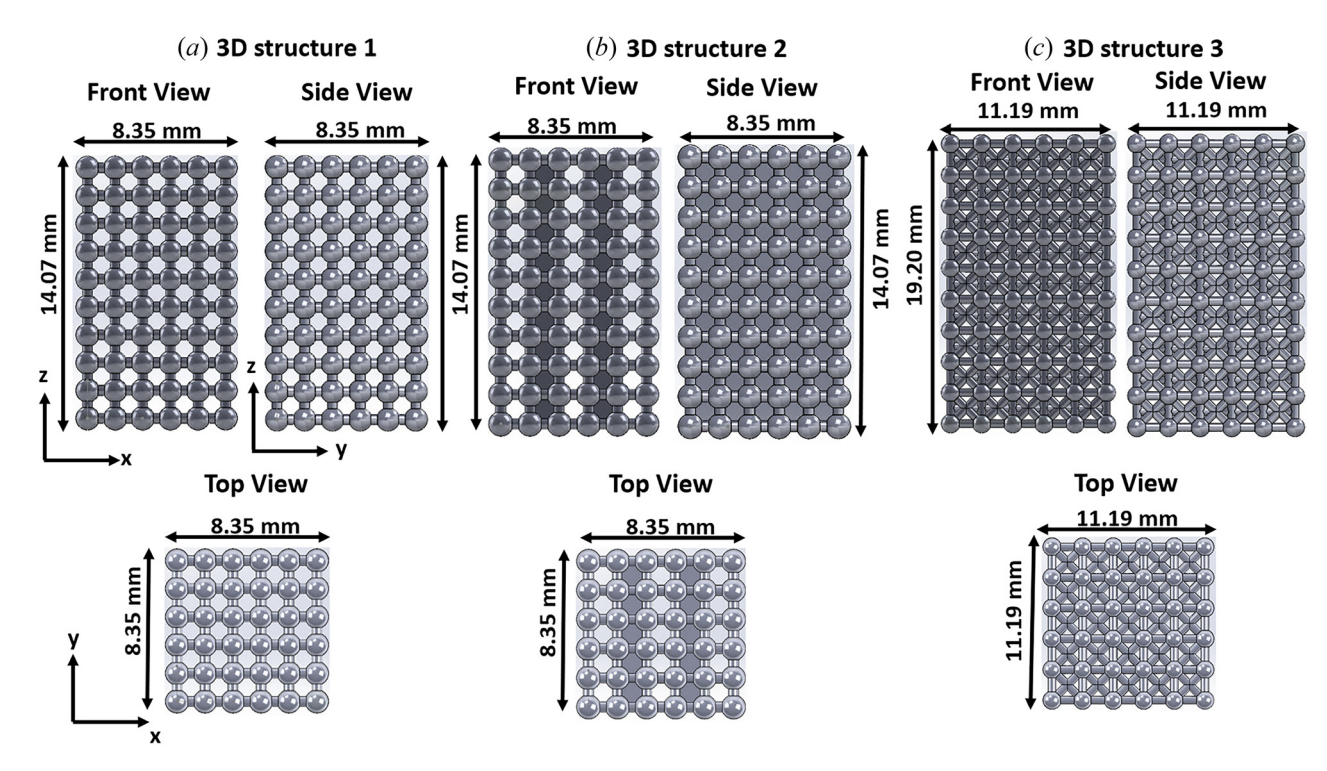


Fig. 1 Front view, side view, and top view of (a) 3D-structure 1 (b) 3D-structure 2, and (c) 3D-structure 3

Table 1 Dimensional specifications of the three additively manufactured porous structures

	3D structure 1	3D structure 2	3D structure 3
Dimension (L, W, H), mm	8.35, 8.35, 14.07	8.35, 8.35, 14.07	11.19, 11.19, 19.2
Porosity, φ (%)	45.87	30.58	33.27
Mass (g)	0.42	0.61	1.31
Effective pore radius (mm)	0.41	0.41	0.16
Number of layers	10	10	10
Number of spheres	360	360	360
Radius of spheres (mm)	0.6	0.6	0.6

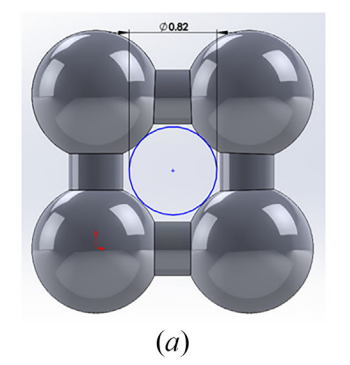
experimental apparatus is divided into three parts: Sec. 2.1 manufacturing process and specifications of additively manufactured porous structures, Sec. 2.2 wettability measurements of the additively manufactured material, and Sec. 2.3 experimental procedures.

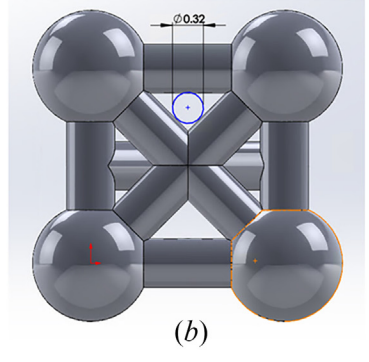
2.1 Manufacturing Parameters and Specifications. The porous structures were designed in SOLIDWORKS 2021 and were manufactured by Protolabs using stereolithography technology (i.e., ± 0.1 mm of thickness resolution). All structures were built with translucent acrylonitrile butadiene styrene (ABS). The front, top, and side views of 3D structures 1, 2, and 3 are pictured in Fig. 1. In 3D-structure-1, 360 1.2-mm-diameter spheres of were stacked in 10 layers with center-to-center spacings of 1.43 mm. The spheres were connected using 0.2-mm-diameter cylinders in the x, y, and zdirections; each layer consisted of 36 spheres. The design specifications of 3D-structure 1 and 2 were similar, except that two layers in 3D-structure 2 in the y-z direction were filled with solid material (i.e., ABS translucent) to restrict lateral interaction of water in x-y direction. As a result, 3D-structure 2 had a higher mass (i.e., 0.61 g) and lower porosity (i.e., 31%) than 3D structure 1. Figure 1 and Table 1 include the dimensional specifications of all additively manufactured porous structures. In 3D-structure 3, 1.2-mmdiameter spheres were used and the center-to-center distances were 2 mm (i.e., a larger spacing than structures 1 and 2). The spheres were connected with 0.2-mm-diameter cylinders in x, y, and z directions. To vary the pore size in z-direction, a horizontal cross shaped structure (built with two cylinders of 0.2-mm-diameter) was incorporated in the middle of each layer. Figure 2 includes the zoomed-in images of unit cell of (a) 3D-structure 1 and 2, and (b) 3D-structure 3. The effective pore radius is measured based on the radius of a circle inscribed inside a pore. Figure 2 also demonstrates the dimension of inscribed circles inside the pores of 3D-structure 1, 2, and 3. For the horizontal cross-shaped structure, the effective pore radius was smaller in 3D-structure 3 (i.e., 0.16 mm) than the 3Dstructure 1 and 2 (i.e., 0.41 mm). The effective pore radius was measured following the inscribed circle method described by Takeuchi et al. [33,34].

2.2 Characterization of Additively Manufactured Material. Translucent ABS material was selected for manufacturing the additively manufactured structures to enable visualization of water during evaporation with a high-speed camera. The material had density of 1.25 g/cm³ with 55 ± 10 MPa of tensile strength [35]. To measure the wettability, a small flat plate (L = 30 mm, W = 30 mm, H = 3 mm) was manufactured from the same material and a 1- μ L deionized water droplet was placed on the top of ABS flat plate with a 0.2–2 μL pipette (Fisherbrand Elite, Waltham, MA). A goniometer was used to measure the contact angle; Fig. 2(c) shows the contact angle of 1- μ L droplet on flat ABS surface; the material is hydrophilic with a static contact angle of 36.93 deg. Figure 3 includes the topview and side-view microscopic images of the three additively manufactured structures. An LSM-5 PASCAL (Zeiss, Oberkochen, Baden-Württemberg, Germany) confocal microscope was used to capture the microscopic images of the 3D-printed structures with $4\times$

magnification.

2.3 Experimental Procedure and Uncertainties. Evaporation of water from additively manufactured structures was conducted at atmosphere pressure with $T_{\rm air} = 22.2\,^{\circ}\text{C}$, 13–17% relative humidity (RH). Figure 4 represents the schematic of experimental setup. Initially, the de-ionized water was placed in a glass beaker (i.e., 2-cm-diameter, 3-cm-height) and equilibrated to room temperature over thirty minutes. Then, the additively manufactured structure was fully submerged in the de-ionized water with tweezers and remained there until all the pores were invaded with water, as determined by visual inspection and mass measurements. Subsequently, the structure with water was placed on the top of a FX-1200i (A&D; Ann Arbor, MI) scale (sensitivity of ± 0.01 g) to record the evaporative mass loss at 15 min time intervals. Five sides (i.e., all sides except the bottom) of the structure were exposed to natural convection, as all of the experiments were conducted without a container. A solar simulator (ABET LS-10500; Milford, CT) was used to apply 1000 W/m² heat flux and a 90 deg beam tuner was used to apply the simulated solar light on the top of the structure. The heat flux was measured with a LI-200R pyranometer (LI-COR Biosciences, Lincoln, NE) (sensitivity of $75 \,\mu\text{A}$ per $1000 \,\text{W/m}^2$). The evaporation phenomenon and drying front propagation during evaporation were visualized and recorded with a Fastec-IL3 high-speed camera (Fastec Imaging, San Diego, CA) at 24 FPS (frame per second) and the total evaporation time was recorded. To observe the temperature profile of the structure during evaporation, a Teledyne FLIR E8-XT infrared camera (Wilsonville, OR) $(320 \times 240 \text{ pixels resolution})$ was used to capture images at 15 min interval. The mass losses were recorded with Rs-MULTISOFTWARE and each experiment was replicated three times (N = 3).





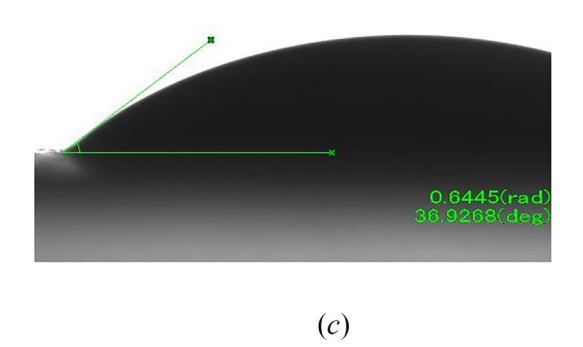


Fig. 2 Zoomed-in image of unit cell of (a) 3D-structure 1 and 2 and (b) 3D structure 3. The circle inscribed in the pore demonstrates the effective pore radius which is 0.41 mm for 3D-structure 1 and 2, and 0.16 mm for 3D-structure 3. (c) Contact angle measurement (36.93 deg) indicates the flat ABS translucent surface is hydrophilic.

3 Results and Discussion

Evaporation phenomena were observed and investigated from three differently designed additively manufactured porous structures. The investigations included evaporative mass loss, drying front propagation during evaporation, analysis of transient saturation, thermal gradient analysis due to evaporation and incident heat flux, evaporation rate, and heat and mass transfer analysis.

3.1 Evaporative Mass Loss. The total initial mass of the 3D structures (i.e., structure and water) and the calculated initial mass of water (i.e., the water holding capacity) of each structure are presented in Table 2. Among the three structures, 3D-structure 3 held more water (i.e., $0.79 \, \mathrm{g}$) than structures 1 and 2 because of their larger size and volume. Additionally, 3D-structure 1 held more water than 3D-structure 2 due to its higher porosity; 3D-structure 2 had two solid-filled layers in the y-z direction which resulted in lowest porosity and lowest water-holding capacity among the three structures. The porosity (i.e., the void fraction of the porous structures) was calculated by the following formulas:

$$\varphi = \frac{V_E}{V_T} \times 100\% = \frac{V_E}{V_E + V_S} \times 100\% \tag{1}$$

where φ is porosity, V_E is the empty volume, V_S is the solid volume, and V_T is the total volume of the 3D printed structure. The porosity was calculated using two methods: (a) based on mass or volume (i.e., Eq. (1)) and (b) using "mass properties" toolbox of SOLIDWORKS. The empty volume was estimated using the mass of the invaded water and the total volume was calculated from the total length, height, and width of the 3D-prinmted structures. Both the values are presented in Table 3. The porosity calculated with Eq. (1) and with SOLIDWORKS,

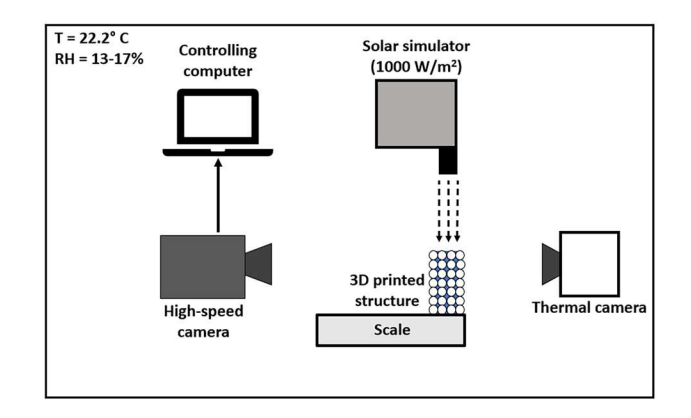


Fig. 4 Schematic diagram of evaporation of water from additively manufactured porous structure

matched well with minimum of 0% to maximum of 3.5% percentage difference.

Figure 5 represents the evaporative mass loss from the structures; each experiment was continued until at least 80% of the total water was evaporated. 3D-structure 3 demonstrated the sharpest decrease, as water evaporated from 0.8 g to approximately 0.1 g within 180 min. 3D-structure 1 and 2 experienced similar trends in evaporative mass loss due to similarity in design specifications (i.e., similar number of spheres, layers, and same pore sizes). Comparing structure 1 and 2, it took more time in structure 1 (i.e., 225 min) to evaporate 0.38 g of water (i.e., 86% of total water) due to greater water holding capacity while 0.28 g (i.e., 88% of total water) was evaporated in 150 min from 3D-structure 2. In previous studies, Shokri et al. [9,10,14,16,17,26] and Lehmann et al. [11] postulated

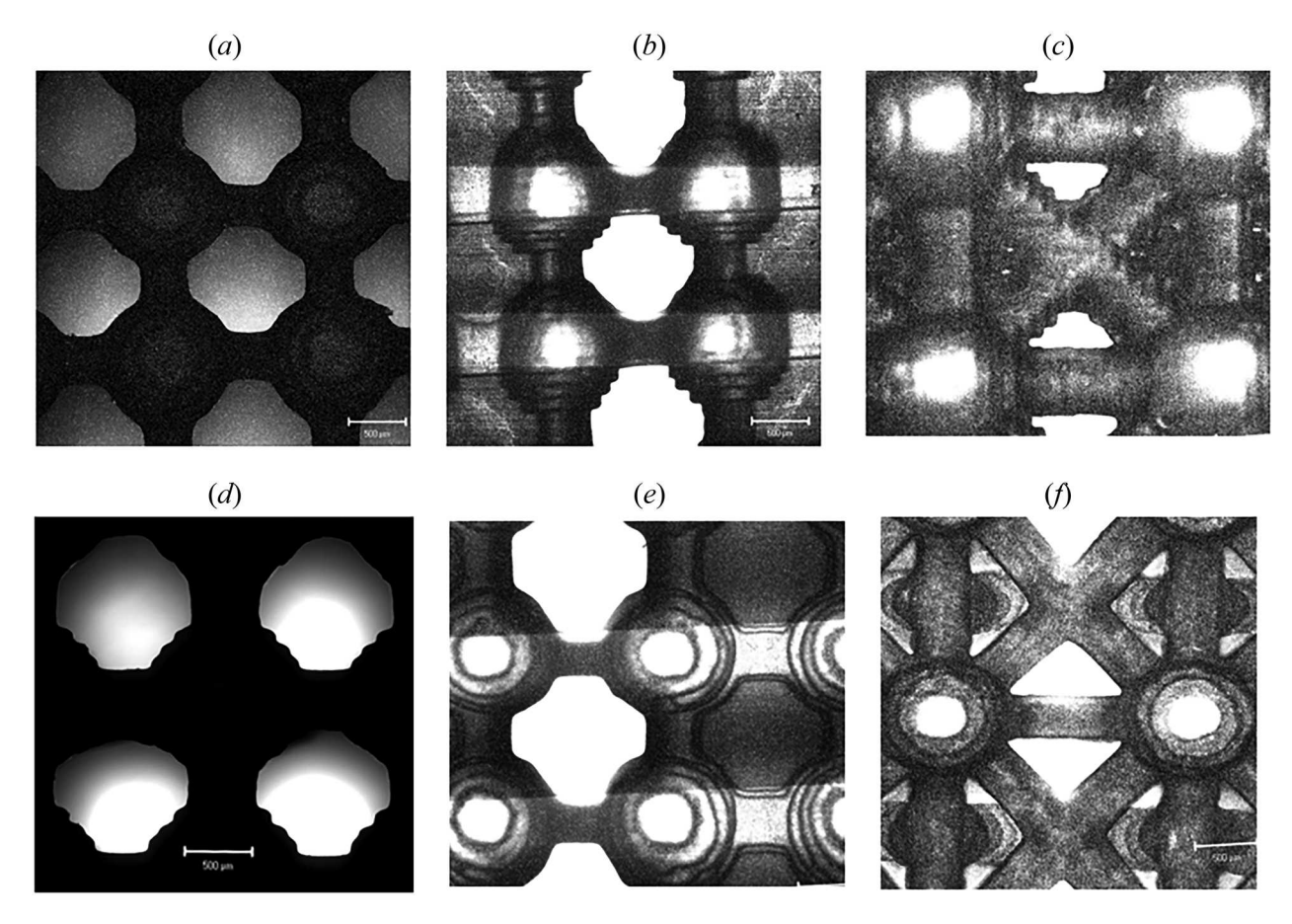


Fig. 3 Microscopic (confocal) images of top view (a-c) and side views (d-f) of 3D-structure 1, 2, and 3 respectively at $4 \times$ magnification

Table 2 Mass properties of three additively manufactured porous structures

Mass	3D structure 1	3D structure 2	3D structure 3
Total initial mass with water (g)	0.87	0.91	2.1
Mass of 3D structure (g)	0.42	0.61	1.31
Initial mass of water (g)	0.45	0.3	0.79

Table 3 Porosity calculation of three additively manufactured porous structures

	3D structure 1	3D structure 2	3D structure 3
Porosity (Eq. (1))	46%	31%	33%
Porosity (SOLIDWORKS) Percentage difference (%)	46% 0	31.5% 1.6	34.2% 3.5

the relationship between pore size and faster evaporation rates. In general, if a porous media has two different pore sizes (r_1 and r_2), and if the pores are interconnected, the liquid will travel from the larger pore to the smaller pore due to capillary action. In a regular cylindrical-shaped porous system, the liquid level drops in the larger pore while it increases in the smaller pore due to capillary action, until the drying front reaches to a certain level called characteristic length. Due to faster movement into smaller pore, the liquid is more susceptible to faster evaporation rate. On the other hand, if a porous media consists of similar sized pores, liquid cannot travel through capillary action, and liquid is evaporated at same rate from all pores due to absence of characteristic length (i.e., $L_c = 0$).

The faster evaporation rate from 3D-structure 3 may be explained by this phenomenon. For the presence of two different-sized pores, more liquid from a larger pore traveled toward a smaller pore, leading to a sharp increase in evaporation rate [Fig. 5(c)]. On the other hand, 3D structures 1 and 2 consisted of similar pore sizes along all three axes, leading to an absence of capillary movement of water. As a result, the capillary potential was limited, resulting in the absence of characteristic length (i.e., $L_c = 0$), and the liquid was evaporated at a same rate from all pores [Fig. 5(b)]. Comparing the pore matrix of all three structures, the faster evaporation from structure 3 compared to structures 1 and 2 is theoretically explained and practically observed.

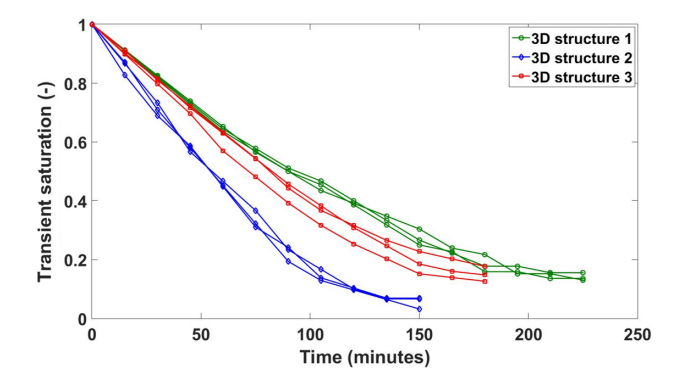


Fig. 6 Transient saturation versus time for all three additively manufactured porous structures

3.2 Transient Saturation and Drying Front Propagation. During evaporation, due to evaporative mass loss, the unsaturated portion in 3D-structures increased with time. The drying front depth is defined as the vertical distance from the top of the unsaturated portion to the saturated part of the porous media. Transient saturation was calculated using the following formula:

$$S = \frac{V_t}{V_i} \tag{2}$$

where V_i is the initial water volume and V_t is the transient volume of water. The transient saturation of water for three structures for all three replications was plotted against time (Fig. 6). The transient saturation decreased gradually for all three additively manufactured structures with time, but 3D-structure 2 experienced the sharpest decrease due to lower initial water volume.

The drying front propagated through the porous structure due to evaporative mass loss and the portion of unsaturated areas increased. In this experiment, the length of drying front increased with time and encapsulated the whole structure. The length of drying front was calculated using the following formula as a function of transient saturation:

$$L_D = H(1 - S) \tag{3}$$

where L_D is the drying front depth, H is the height of the porous structure, and S is the transient saturation of the porous medium. The

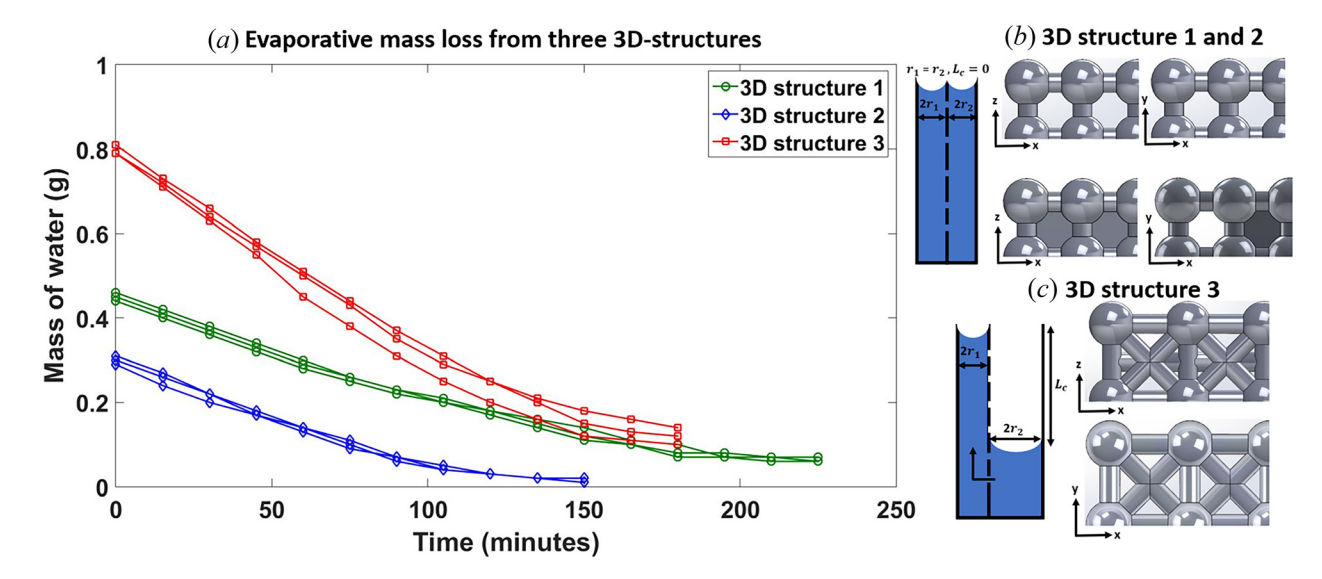


Fig. 5 (a) Evaporative mass loss of water from three additively manufactured porous structures, (b) uniform porous matrix leading to absence of characteristic length in 3D structure 1 and 2, (c) nonuniform porous matrix in 3D structure 3 leading to presence of characteristic length and faster evaporation rate due to capillary action

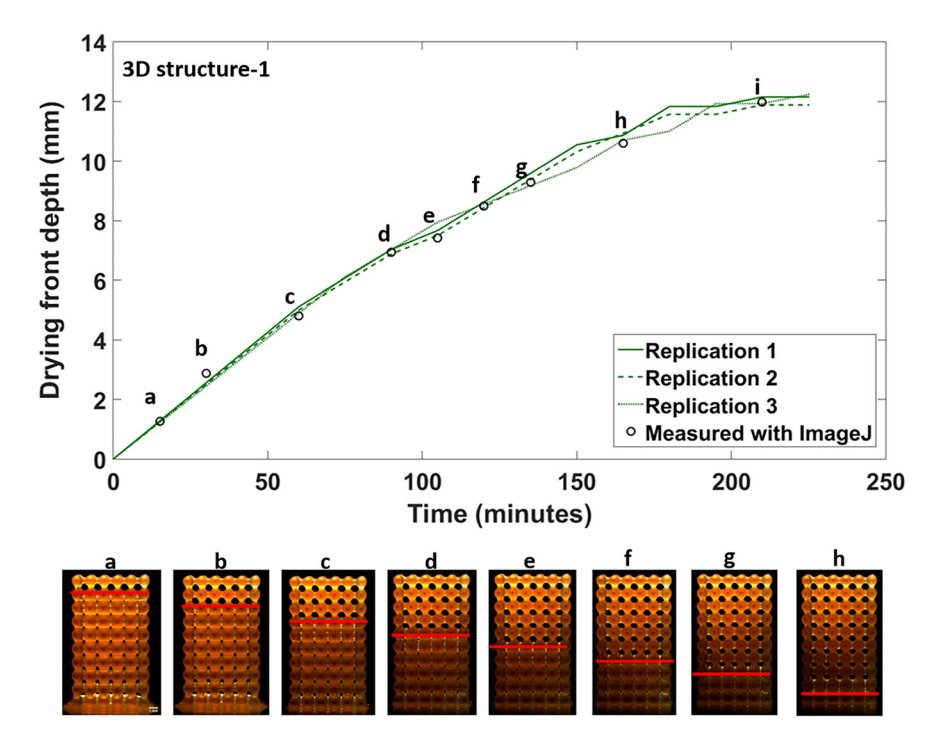


Fig. 7 Drying front depths during evaporation from 3D-structure 1

drying front depths, calculated using the previous equation as a function of transient saturation, were plotted against time for three replications for all three additively manufactured structures (Figs. 7–9). For all three structures, the drying front depths increased with time as the portion of unsaturated areas increased and encapsulated the whole structure. Drying front depths were also measured with images captured with the high-speed camera. The depths were measured with IMAGEJ after complete evaporation of water from a layer and that depths were also plotted in the same graph (Figs. 7–9). The drying front depths measured as a function of transient

saturation and measured from the images matched significantly for all three 3D-structures.

3.3 Evaporation Rate Modeling (Steady State, Constant Rate Period). The evaporation rates (i.e., $\frac{dm}{dt}$) were calculated from the mass loss data (Fig. 5). Consequently, a layer-by-layer coupled heat and mass transfer model was formulated based on different layers of the porous structures. The following assumptions were made to simplify the predictive model:

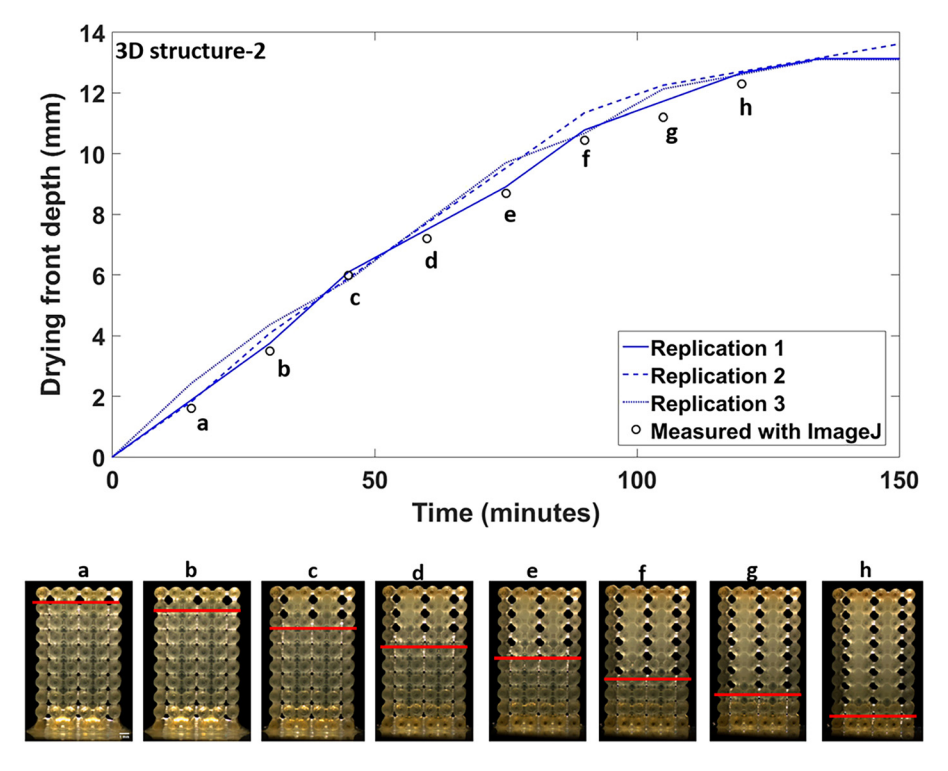


Fig. 8 Drying front depths during evaporation from 3D-structure 2

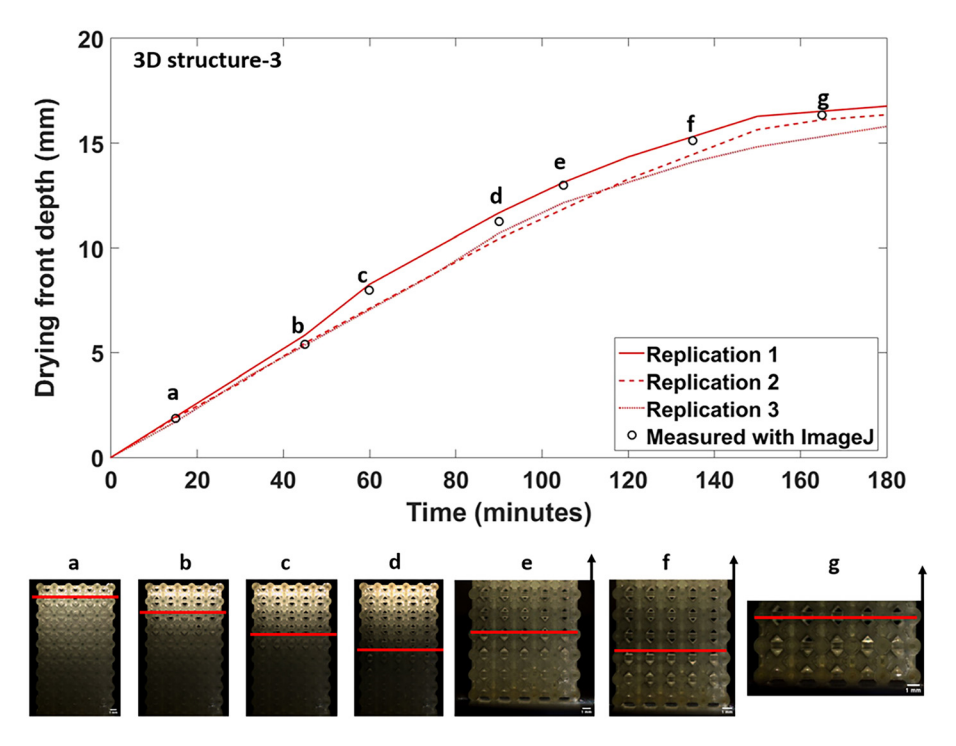


Fig. 9 Drying front depths during evaporation from 3D-structure 3. To get better views, at later stage of evaporation, the camera was zoomed to the lower part of the structure. The arrow sign represents the presence of upper half of the structure.

- (a) Steady-state.
- (b) Energy balance was considered only in the vertical direction of the porous structure.
- (c) In each layer, the additively manufactured material and water were assumed to be in isothermal state.
- (d) Energy and mass loss from the sides were assumed negligible.
- (e) The temperature of the porous structure during evaporation was measured and recorded with a thermal camera and the subsequent layer temperature was estimated from the thermal images and since, all the structures were almost similar in design specifications, similar thermal gradients were assumed for all three structures during evaporation.

Figure 10 demonstrates the energy balance, assuming the steadystate in a single layer of the porous structure. Here, \dot{Q}_{evap} is the evaporative heat flux, \dot{Q}_{solar} is the incident solar heat flux, \dot{Q}_{conv} is the convective heat flux, \dot{Q}_{cond} is conductive heat flux between layers, \dot{Q}_{abs} is the absorbed heat flux and \dot{Q}_{ref} is reflected heat flux.

The following equation was used to express the energy balance on the porous structure with water in the pores:

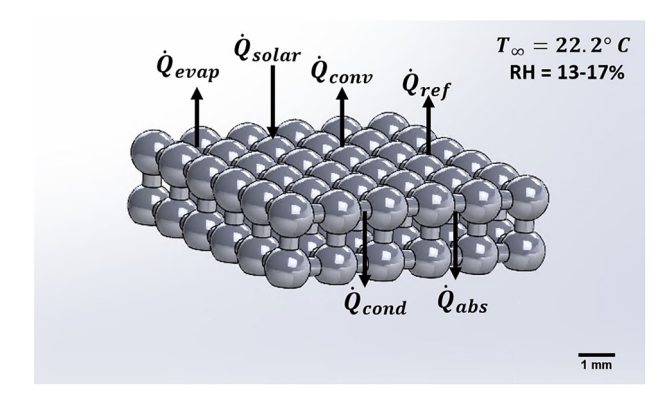


Fig. 10 Steady-state heat transfer in a single layer of the porous structure

$$(1 - \varphi)A\alpha \dot{Q}_{\text{solar}}$$

$$= A (1 - \varphi) \frac{\sigma(T_s^4 - T_\infty^4)}{\left[\frac{1}{\epsilon_s} + \frac{1}{\epsilon_a} - 1\right]} + A\varphi \frac{\sigma(T_w^4 - T_\infty^4)}{\left[\frac{1}{\epsilon_w} + \frac{1}{\epsilon_a} - 1\right]}$$

$$+ h_{\text{conv}}A\varphi(T_w - T_\infty) + K_{\text{eff}}A\left(\frac{T_s - T_B}{L}\right) + \dot{m}\varphi h_{lg}$$
 (4)

where φ is the porosity, A is the surface area of the top layer of the porous surface, α is the absorptivity of the porous structure, Q_{solar} is the applied heat flux by solar simulator, σ is the Stefan-Boltzman constant, T_s is the surface temperature, T_w is the water temperature, T_∞ is the ambient temperature, \in is the emissivity of the porous structure, \in is the emissivity of air, h_{conv} is the convective heat transfer coefficient, T_w is the water temperature, K_{eff} is the effective thermal conductivity, T_B is the bottom temperature of single layer, L is the single layer thickness, \dot{m} is the evaporation rate, and h_{lg} is the latent heat of vaporization. The effective thermal conductivity is expressed as follows:

$$K_{\text{eff}} = (1 - \varphi)K_s + \varphi K_w \tag{5}$$

where K_s is the thermal conductivity of the porous material and K_w is the thermal conductivity of water. To calculate the convective heat transfer coefficient, the following Darcy-modified equation was used to calculate Rayleigh number [23]

$$Ra_x = \frac{g\beta k(T_w - T_\infty)x}{v_a \alpha_m}$$
 (6)

where Ra_x is the Darcy-modified Rayleigh number, g is the acceleration due to gravity, β is the thermal expansion coefficient, k is the intrinsic permeability of the porous medium, x is the length of the porous top surface, v_a is the kinematic viscosity of air, and α_m is the thermal diffusivity. The intrinsic permeability is expressed as follows:

$$k = 0.01 \, \varphi \, r_{\rm eff}^{\,2} \tag{7}$$

Table 4 Common parameters to model the steady-state evaporation rate

Ambient temperature, T_{∞}	22.2 °C
Applied heat flux, $\dot{Q}_{\rm solar}$	1000W/m^2
Absorptivity, α	0.98
Stefan-Boltzmann constant, σ	$5.67 \times 10^{-8} \text{ W/m}^2 \text{K}^4$
Emissivity of solid surface, \in_s	0.92
Emissivity of air, \in_a	0.85
Emissivity of water, \in_{w}	0.96
Thermal conductivity of solid, K_s	0.163 W/m K
Thermal conductivity of water, K_w	0.6049 W/m K
Thermal conductivity of air, K_a	0.02529 W/m K
Thermal expansion coefficient, β	$0.003405\mathrm{K^{-1}}$
Kinematic viscosity of air, v_a	$8.63 \times 10^{-8} \text{ m}^2/\text{s}$

Table 5 Temperature and heat flux in different layers of the additively manufactured structures

Layers	Temperature $(T_s = T_w), K$	Heat flux ($\dot{Q}_{solar/A}$), W/m
1	297	1000
2	298	990
3	298	980
4	299	970
5	299	960
6	300	950
7	301	940
8	302	930
9	302	920
10	302	910

where φ is porosity and $r_{\rm eff}$ is effective pore radius. The following Raleigh-Nusselt correlation was used to calculate the Nusselt number for laminar flow [36]:

$$Nu = 0.413 \,Ra^{\frac{1}{3}} \tag{8}$$

$$h_{\rm conv} = \frac{Nu K_a}{r} \tag{9}$$

where Nu is the Nusselt number, $h_{\rm conv}$ is the convective heat transfer coefficient, and K_a is the thermal conductivity of air. Since all the 3D structures were manufactured with same material (i.e., ABS plastic), the common parameters to estimate steady-state evaporation rate are presented in Table 4.

For evaporation rate calculations, the temperature of each layer was measured from the images captured with the thermal camera at 15 min intervals. For the first layer, the top layer of the porous structure was considered as the surface temperature, T_s . Subsequently, after the evaporation of water from first layer, the temperature of the second layer was considered as the surface temperature (i.e., T_s) and they were determined from the thermal images Fig. 11). The similar procedures were followed until the water reached to the last layer (i.e., 10th layer). Since all the three structures were manufactured with similar material (i.e., translucent ABS) and the design specifications were almost similar, the thermal gradients during evaporation exhibited similar trends. For each layer, the material and water were assumed to be in thermal equilibrium (i.e., $T_s = T_w$), and for each layer the subsequent parameters such as $K_{\rm eff}$, Ra, k, Nu, and $h_{\rm conv}$ were calculated. In different layers, the heat flux, the surface temperature, water temperature, and bottom temperature changed. At the last two layers (i.e., 9th and 10th layers), the temperatures were similar (e.g., with approximately 0.5 K temperature difference), and thus they were considered to be in equilibrium with eighth layer's temperature. Figure 11 demonstrates the layer-by-layer thermal gradient during evaporation from 3D structure-1.

The solar heat flux in each layer was measured with pyranometer. The heat flux was measured at three points [i.e., at the top (layer 1), at the middle (layer 5), and at the bottom (layer 10)], and by simple interpolation, the heat flux in each layer was estimated. Table 5 represents the temperature and incident solar heat flux in each layer of the additively manufactured structures. For all structures, the temperature and heat fluxes were assumed to be similar in each layer. For each layer, the evaporation rate was calculated using the following equation:

$$\dot{m}_{i..n} = \left[(1 - \varphi) A \alpha \dot{Q}_{\text{solar}i..n} - A (1 - \varphi) \frac{\sigma \left(T_{si..n}^4 - T_{\infty}^4 \right)}{\left[\frac{1}{\epsilon_s} + \frac{1}{\epsilon_a} - 1 \right]} - A \varphi \frac{\sigma \left(T_{wi..n}^4 - T_{\infty}^4 \right)}{\left[\frac{1}{\epsilon_w} + \frac{1}{\epsilon_a} - 1 \right]} - h_{\text{conv}} A \varphi \left(T_{wi..n} - T_{\infty} \right) - K_{\text{eff}} A \left(\frac{T_{si..n} - T_{Bi..n}}{L} \right) \right] / \varphi h_{lg}$$

$$(10)$$

where i is layer 1 and n is layer 10. Due to the small distance between top and bottom surface of each layer (i.e., 1.43 mm for 3D structure-1 and -2, and 2 mm for 3D structure-3), the temperature difference (i.e., $T_s - T_B$) was measured as 0.5 K for each layer.

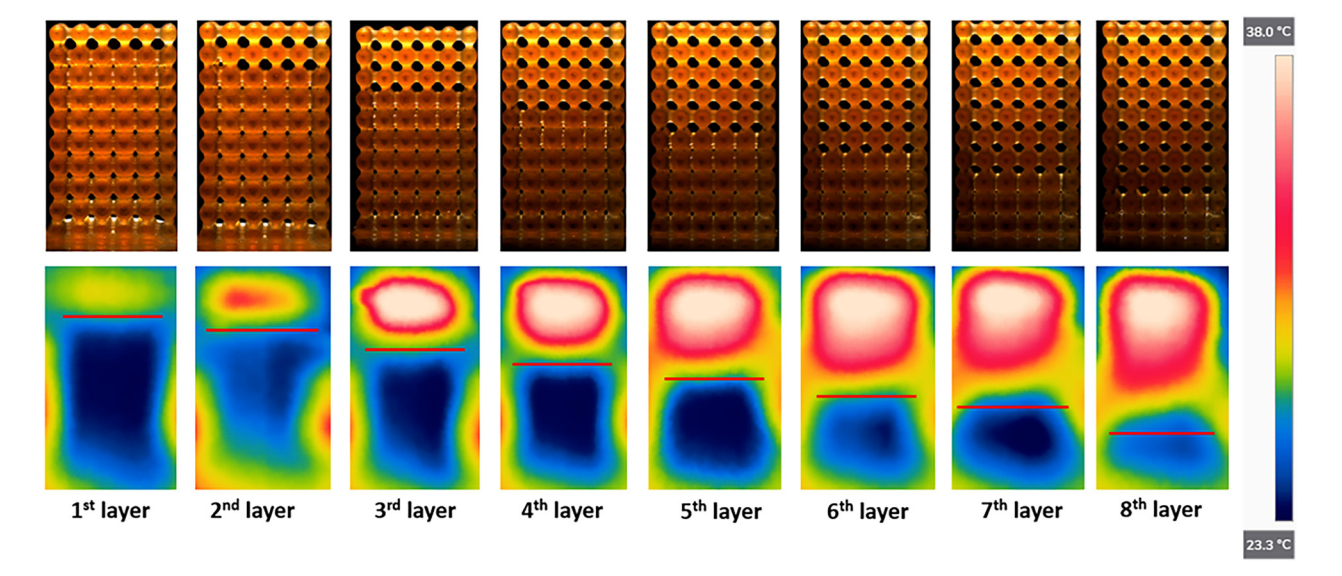


Fig. 11 Layer-by-layer thermal gradient while evaporation of water from additively manufactured structure-1

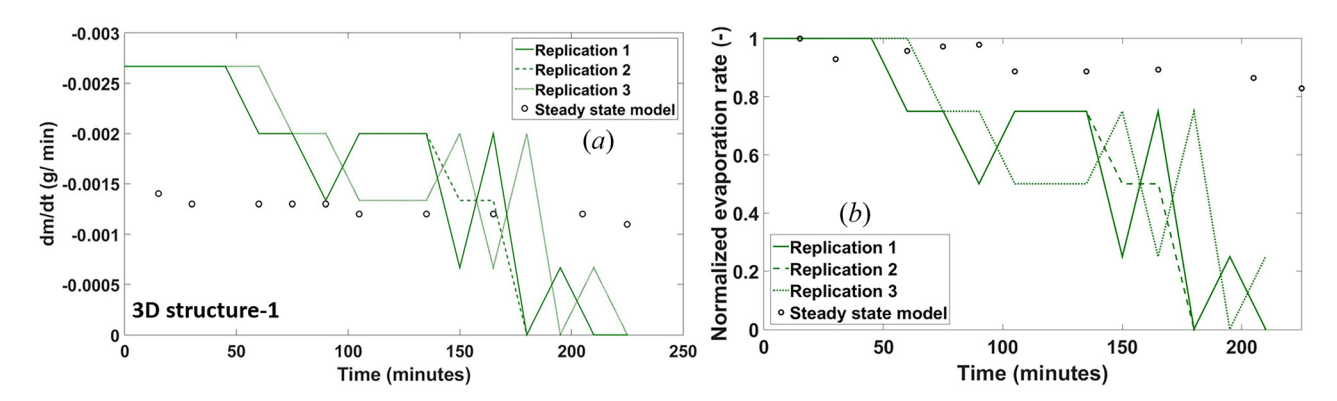


Fig. 12 (a) evaporation rate (dm/dt) and (b) normalized evaporation rate versus time for 3D-structure 1

Evaporation rates for all three 3D structures were plotted against time and are demonstrated in Figs. 12-14(a). The normalized evaporation rate was calculated by dividing the transient evaporation rate by the maximum evaporation rate [Figs. 12-14(b)]. All the three structures experienced a certain time (i.e., approximately 60-80 min) of constant rate period evaporation and then experienced a decrease in evaporation rate (i.e., falling rate of evaporation). The highest evaporation rate was found in 3Dstructure 3 (approximately 0.005 g/min) and it continued until 80 min of total evaporation time. The larger evaporation rate was associated with larger surface area (i.e., 125.21 mm²) and smaller effective pore size (i.e., 0.16 mm), which resulted in extended period of constant evaporation rate. The evaporation rate in constant rate period was similar for 3D-structure 1 and 2 (i.e., 0.0025-0.003 g/min). Due to larger void fraction, 3D-structure 1 held more water than the others resulting in longest evaporation time (i.e., approximately 250 min).

The analytical evaporation rate calculated from the steady-state energy balance equation was plotted in the same graph (Figs. 12–14). The analytical and experimental results matched well for all three 3D-structres during the constant period of evaporation. Evaporative mass loss with application of external heat flux is a complex transient phenomenon that was not considered in the model assumption. So, at the later stages of evaporation (i.e., the falling rate of evaporation), the data did not match with the experimental results as the falling rate period of evaporation is a transient process and the model had limitations in predicting the transient phenomena. The falling rate period of evaporation was predicted by another model in Sec. 3.4.

Though 3D-structure 1 and 2 had similar initial evaporation trends, the overall evaporation trends were not similar. After approximately 60 min, in 3D-structure-2, evaporation experienced a significant decrease compared to 3D-structure-1. The restriction of lateral water movement could be one of the contributing factors leading to decrease in evaporation rate in 3D-structure 2. Previous

research [6,9,11,14,17,37] postulated that the presence of thin liquid films or liquid islands contributes to formation of hydraulic linkages throughout the porous structure, which leads to extended period of constant rate period or smaller decrease in initial evaporation rates. In 3D-structure 2, thin liquid islands created in partially saturated parts could not create linkage with water laterally which resulted in steep decrease in evaporation rate.

Figure 15 demonstrates the 2D view of all 3D structures and illustration of evaporation front and water movement. In 3Dstructure-1 [Figs. 15(a)–15(c)], the pore sizes are uniform, and all the pores are interconnected. While evaporating, water created a continuous liquid linkage from the saturated part to the unsaturated part by forming tiny liquid islands. Shokri et al. [17,26] demonstrated the presence of two evaporation fronts: primary and secondary while evaporating from porous media where liquid islands are formed. Though the primary water level drops down with primary evaporation front, the liquid still maintains a hydraulic linkage with the unsaturated part, and water evaporates from the secondary evaporation front exposed to the air. In 3D-structure 1, it is postulated that due to formation of liquid islands, the evaporation rate was almost constant throughout the entire period. After maintaining a constant period (i.e., 0-60 min), the evaporation rate dropped down and again maintained a constant rate (i.e., ~90 to 180 min), irrespective of other two structures due to presence of two drying fronts simultaneously.

In 3D-structure-2 [Figs. 15(d)–15(f)], the lateral liquid movement was restricted with a solid fill between two layers in the y–z direction, and it is postulated that this lead to the formation of fewer liquid islands and an absence of hydraulic linkages. When the water level dropped down due to evaporative loss, the primary evaporation front dropped down as well, and the evaporation experienced a sharp decrease due to absence of secondary evaporation front. In 3D structure-3 [Figs. 15(g)–15(i)], the movement of water is dominated by capillary action due to presence of two different-sized pores [Fig. 15(c)]. The upward movement of water is obstructed by gravity

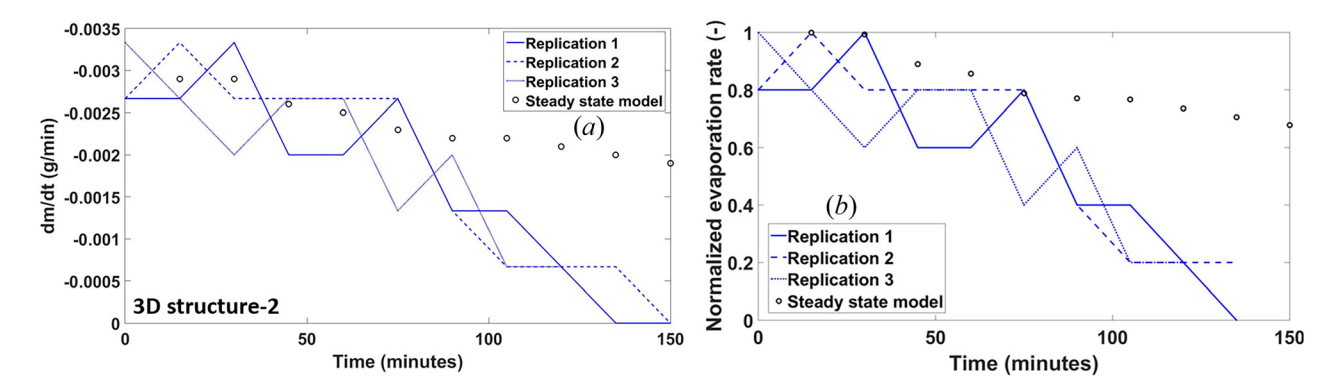


Fig. 13 (a) evaporation rate (dm/dt) and (b) normalized evaporation rate versus time for 3D-structure 2

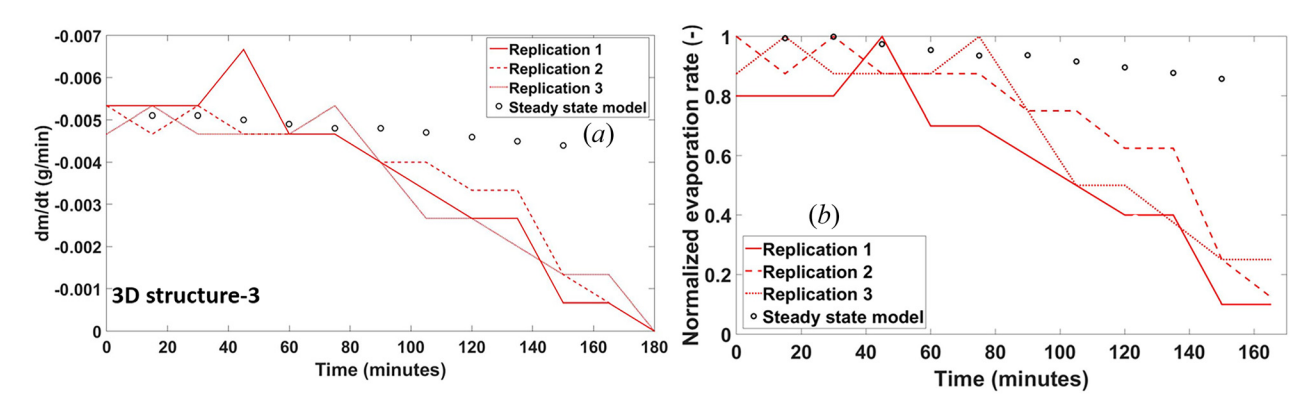


Fig. 14 (a) evaporation rate (dm/dt) and (b) normalized evaporation rate versus time for 3D-structure 3

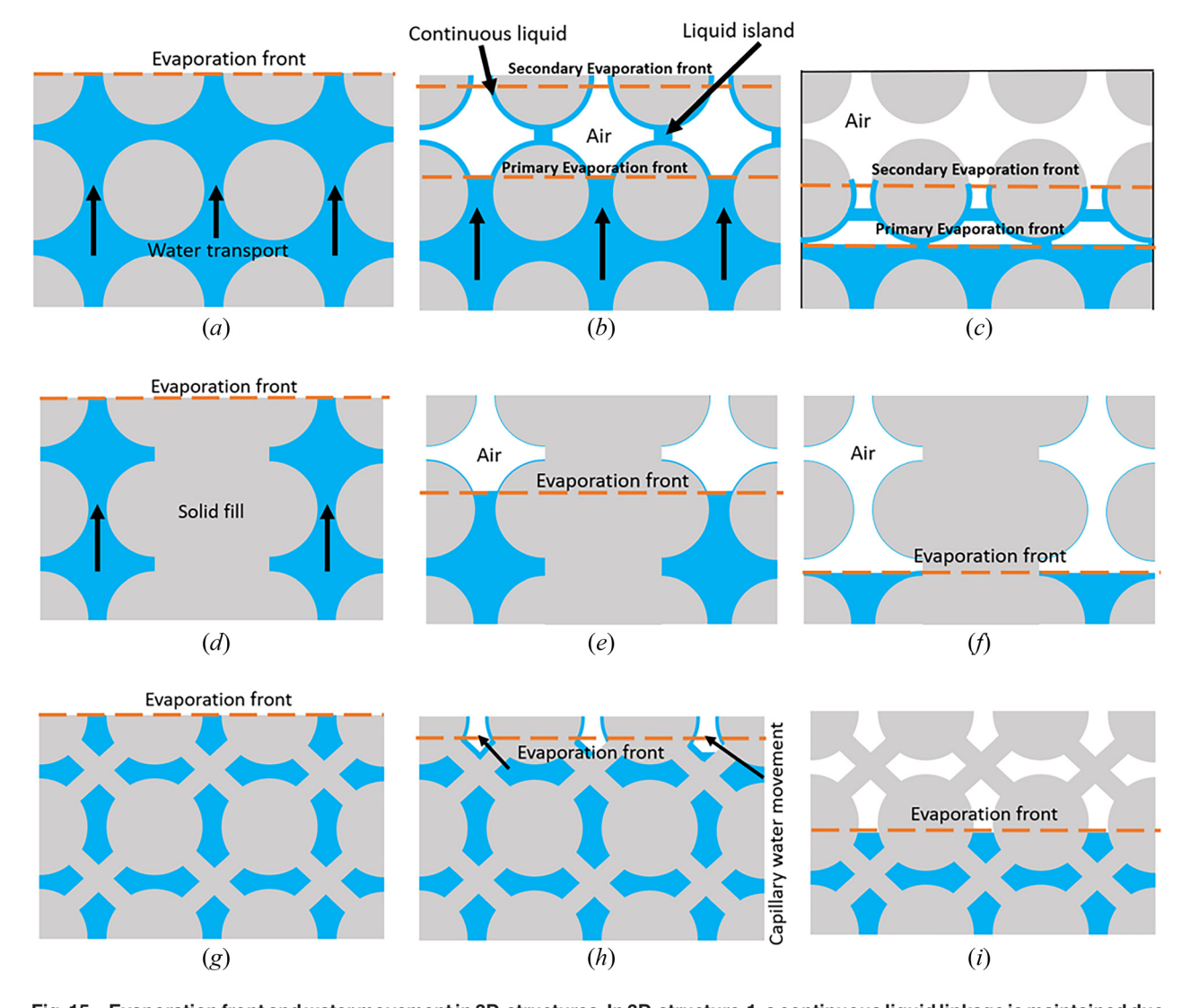


Fig. 15 Evaporation front and water movement in 3D-structures. In 3D-structure-1, a continuous liquid linkage is maintained due to formation of liquid islands and lateral movement of water (a-c). In 3D-structure-2, water evaporates gradually, and fewer liquid islands are formed due to restricted lateral movement (d-f). In 3D-structure-3, water evaporation is dominated by capillary action and when the capillary action cannot overcome gravity, evaporation rate starts to drop.

acting in the opposite direction. When the capillary force was dominated by gravity, the upward water movement stopped, and the evaporation experienced a sharp decrease similar to 3D structure-2.

3.4 Modeling of Falling Rate Period of Evaporation. The previous modeling was based on steady-state, and the model

matched well with the experimental data at the beginning (i.e., the constant rate period of evaporation). When evaporation entered into the falling rate of evaporation, the experimental data did not match well with the model due to lack of insufficiency in assumption (i.e., steady-state versus transient). Previous researchers estimated and modeled the falling rate period of evaporation from porous

Table 6 Parameters to estimate falling rate period evaporation rate

Radius of single particle, r_0 (mm) Diffusion coefficient, D (m^2/s)	$0.6 \\ 2.54 \times 10^{-5}$
Thermal diffusivity, α (m ² /s)	0.00002105
Density of water, ρ (kg/m ³)	997

structures where the water starts to detach from the porous material (i.e., rupture and formation of liquid island) and completely dry regions (i.e., unsaturated part) start to build up in the upper portion of the porous media. Evaporation rate in this stage acts as a function of drying front depth and based on this assumption the normalized evaporation rate for falling rate period is expressed as following by Yiotis et al. [21,22]:

$$\dot{e} = \frac{1}{1 - kx_i} \tag{11}$$

where \dot{e} is the normalized evaporation rate at falling rate period, $k=\frac{\mathrm{Sh}}{r_0}$, Sherwood number, $\mathrm{Sh}=\frac{D_M}{D_{\mathrm{eff}}\delta_m}$, D_M is the apparent diffusion coefficient, D_{eff} is the effective diffusion coefficient, δ_m is the thermal boundary layer thickness, r_0 is the radius of single particle, and x_i is the drying front depth with time. To estimate the effective diffusion coefficient, the following correlation was used expressed by Dullien [38], Acrivos and Chang [39], and Park et al. [40]:

$$D_{\text{eff}} = D_M \left[1 - 3 \frac{(1 - \varphi)}{2} + 3(0.89) \frac{(1 - \varphi^2)}{4} \right]$$
 (12)

where ϕ is the porosity. The model is based on the following assumptions:

- (a) The model is valid when evaporation takes place while forming of liquid islands by rupture of continuous hydraulic linkages
- (b) Evaporation takes place on the intersection of saturated and unsaturated parts, i.e., the drying front
- (c) The unsaturated part is considered to be completely dry irrespective of presence of tiny liquid islands

To estimate the mass boundary layer thickness, the following correlations were implemented [27]:

$$\delta_m = \delta_T \operatorname{Le}^{\frac{1}{3}} \tag{13}$$

$$\delta_T = \frac{L^*}{Nu} \tag{14}$$

$$Le = \frac{\alpha_m}{D} \tag{15}$$

where δ_m is the mass boundary layer thickness, δ_T is the thermal boundary layer thickness, Le is the Lewis number, L^* is the center-to-center distance of the particles, Nu is the Nusselt number, α_m is the thermal diffusivity of air and D is the diffusion coefficient. Parameters shown in Table 6 were used to estimate the falling rate period model. In these experiments, both 3D-structures 2 and 3 experienced significant decreases in evaporation rates after the termination of the constant rate period. The falling rate period started approximately after 60 min and 75 min, respectively, for 3D-structure 2 and 3 and the time period was specified from the experimental evaporation rate graph. For 3D-structure 1, due to presence of continuous liquid films, the constant rate period was prolonged, and it experienced very short period of falling rate of evaporation; thus, structure 1 was not considered for this falling rate modeling. To estimate experimental normalized evaporation rate,

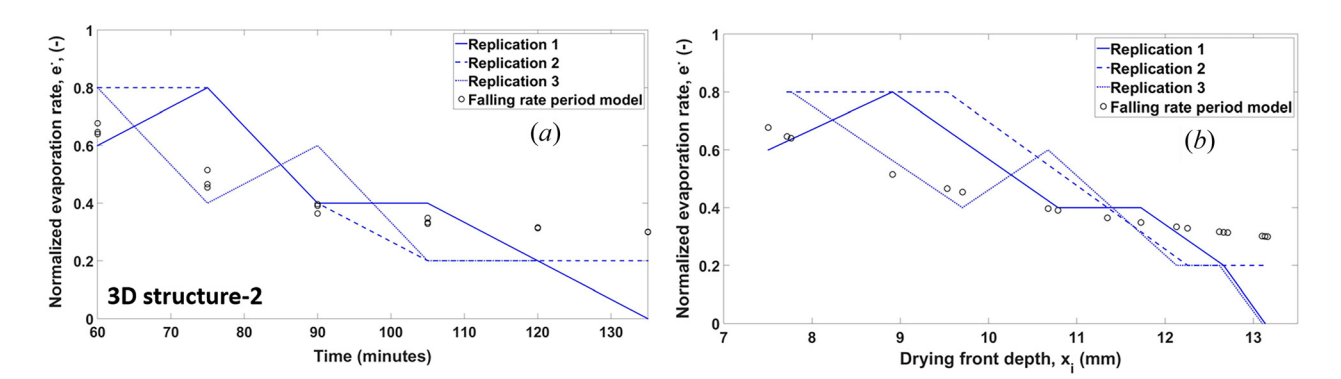


Fig. 16 Normalized evaporation rate versus (a) time and (b) drying front depth during falling rate period for 3D-structure 2. The analytical model and experimental data matched well during falling rate period of evaporation.

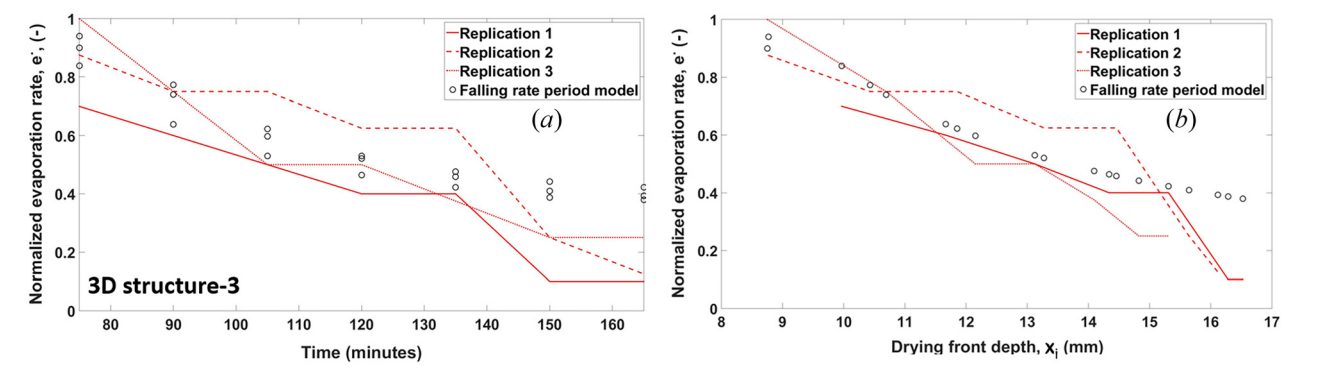


Fig. 17 Normalized evaporation rate versus (a) time and (b) drying front depth during falling rate period for 3D-structure 3. The analytical model and experimental data matched well during falling rate period of evaporation.

the evaporation rates (i.e., dm/dt) were divided by maximum evaporation rate using the following equation [21]:

$$e_{\text{norm}} = \frac{\left(\frac{dm}{dt}\right)_i}{\left(\frac{dm}{dt}\right)_{\text{max}}} \tag{16}$$

where $e_{\rm norm}$ is the experimental normalized evaporation rate, $\left(\frac{dm}{dt}\right)_i$ is the evaporation rate at a particular time and $\left(\frac{dm}{dt}\right)_{\rm max}$ is the maximum evaporation rate throughout the evaporation process. The calculated normalized evaporation rate from the experimental data and the modeled normalized evaporation rate (\dot{e}) were plotted against (a) time and (b) drying front depths for both 3D-structure 2 (Fig. 16) and 3 (Fig. 17). For both the 3D-structures, the experimental evaporation rate matched significantly with the falling rate period model.

4 Conclusions

Three additively manufactured porous structures of different design specifications were manufactured with translucent ABS materials to study evaporation and drying front propagation with application of external source of heat flux. To visualize the drying front propagation and thermal gradients, a high-speed camera and a high-resolution thermal camera were used to capture images at 15 min time intervals. The evaporative mass loss from the porous structures was recorded with a sensitive scale and the evaporation rate was calculated as a function of evaporative mass loss. A steadystate heat-mass transfer model was established to predict the evaporation rates. 3D-structure 3 experienced the sharpest decrease in the mass loss as the water evaporated from 0.8 g to 0.1 g within 180 min. Though structures 1 and 2 were almost similar in design, the inclusion of lateral liquid interaction due to solid fill in y-z direction in structure 2 made it significantly different than structure 1. Due to lateral motion of water, more liquid islands were formed in structure 1 leading to creation of continuous hydraulic linkage which resulted in extended period of constant rate period. As a result, after the surface evaporation (i.e., 0-60 min), the evaporation rate dropped down a bit when liquid islands started to form in upper layers and again maintained a constant rate period from 90 to 180 min due to formation of hydraulic linkage contrary to structure 2. In structure 2, constant rate of evaporation was dominated by surface evaporation (until \sim 75 min) and the evaporation dropped (i. e., entered into falling rate period) when the hydraulic linkage broke due to restriction in lateral water movement. In 3D-structure 3, the movement of water was dominated by capillary action as water transported from larger pores to smaller pores and the constant rate of evaporation lasted for \sim 75 min. When the water level dropped down due to evaporative loss, the capillary action was restricted by reverse acting gravity and after 75 min, falling rate period of evaporation started.

The drying front depths were calculated as a function of transient saturation and were also measured from the high-resolution evaporation images and plotted against time. The calculated and measured drying front depths matched well representing the correlation between transient saturation and evaporation rate. The steady-state heat and mass transfer coupled modeling matched well in 3D-structure 2 and 3, when the evaporation was in constant rate period (i.e., ~0 to 75 min). In 3D-structure 1, due to continuous liquid linkage and breakup of liquid islands, there were two part of constant rate period: one due to surface evaporation (0-60 min), then the evaporation rate dropped and again maintained a constant rate (i.e., 90-180 min) due to continuous hydraulic linkages. The steadystate model matched well with second part of constant rate period. For predicting the falling rate of evaporation, normalized evaporation rate model was applied in this study and during falling rate of evaporation (i.e., from 75 min to rest of evaporation), the calculated evaporation rate (i.e., the analytical modeling) matched well with experimental results for 3D-structure 2 and 3. Due to prolonged

constant rate of evaporation, 3D-structure 1 experienced very short period of falling rate of evaporation and was not considered for transient modeling. The future works could include establishing a transient model of heat and mass transfer that can predict all the evaporation stages from porous structures. Also, the contribution of liquid island formation during evaporative drying from additively manufactured structures could be another important phenomenon to investigate to understand the water dynamics.

Acknowledgment

We would like to acknowledge Emily Stallbaumer-Cyr for assistance in capturing microscopic images of the 3D-printed structures.

Funding Data

- Directorate for Engineering, National Science Foundation (Grant No. 1651451; Funder ID: 10.13039/100000084).
- Division of Graduate Education, National Science Foundation (Grants No. 1828571; Funder ID: 10.13039/100000082).

Data Availability Statement

The datasets generated and supporting the findings of this article are obtainable from the corresponding author upon reasonable request.

Nomenclature

```
A = \text{surface area (mm}^2)
```

 $D = \text{diffusion coefficient (m}^2/\text{s})$

g = acceleration due to gravity (m/s²)

H = height of porous structure (mm)

 $h_{\text{conv}} = \text{convective heat transfer coefficient (W/m}^2\text{K})$

 h_{lg} = latent heat of vaporization (KJ/kg)

 $\vec{k} = \text{intrinsic permeability (mm}^2)$

K = thermal conductivity (W/m K)

 $K_{\text{eff}} = \text{effective thermal conductivity (W/m K)}$ $K_s = \text{thermal conductivity of water (W/m K)}$

 K_s = thermal conductivity of water (W/m K) K_w = thermal conductivity of solid structure (W/m K)

L = single layer thickness (mm)

 $L_c = \text{characteristic length (mm)}$

 L_e = Lewis number

LD = drying front depth (mm)

 $\dot{m} = \text{evaporation rate (g/min)}$

Nu = Nusselt number

 $Q = \text{heat flux (W/m}^2)$

 $r_1, r_2 = \text{pore radius (mm)}$

Ra = Rayleigh number

 $Ra_x = Darcy$ -modified Rayleigh number

RH = relative humidity (%)

S =transient saturation

Sh = Sherwood number

 $T_w = \text{water temperature (°C)}$

 T_{∞} = ambient temperature (°C)

 $V = \text{volume (mL or mm}^3)$

 $\alpha = absorptivity$

 α_m = thermal diffusivity (m²/s)

 β = thermal expansion coefficient (K⁻¹)

 δ = boundary layer thickness

 $\varepsilon = \text{emissivity}$

 $\rho = \text{density} (\text{Kg/m}^3)$

 $\sigma = \text{Stefan-Boltzman constant } (5.67 \times 10^{-8} \text{ W/m}^2\text{K}^4)$

 $v = \text{kinematic viscosity (m}^2/\text{s})$

 $\varphi = \text{porosity}(\%)$

References

 Kobayashi, Y., Ikeda, S., and Iwasa, M., 1996, "Evaporative Heat Transfer at the Evaporative Section of a Grooved Heat Pipe," J. Thermophys. Heat Transfer, 10(1), pp. 83–89.

- [2] Singh, R., Akbarzadeh, A., Dixon, C., and Mochizuki, M., 2007, "Novel Design of a Miniature Loop Heat Pipe Evaporator for Electronic Cooling," ASME J. Heat Mass Trans., 129(10), pp. 1445–1452.
- [3] Murshed, S. S., and De Castro, C. N., 2017, "A Critical Review of Traditional and Emerging Techniques and Fluids for Electronics Cooling," Renewable Sustainable Energy Rev., 78, pp. 821–833.
 [4] PastUkhov, V. G., Maidanik, Y. F., Vershinin, C., and Korukov, M., 2003,
- 'Miniature Loop Heat Pipes for Electronics Cooling," Appl. Therm. Eng., 23(9), pp. 1125-1135.
- [5] Khrustalev, D., 2002, "Loop Thermosyphons for Cooling of Electronics," Proceedings of Eighteenth Annual IEEE Semiconductor Thermal Measurement and Management Symposium, IEEE, San Jose, CA, Mar. 12-14, pp. 145-150.
- [6] Cho, K. T., and Mench, M. M., 2010, "Fundamental Characterization of Evaporative Water Removal From Fuel Cell Diffusion Media," J. Power Sources, 195(12), pp. 3858-3869.
- Chapuis, O., Prat, M., Quintard, M., Chane-Kane, E., Guillot, O., and Mayer, N., 2008, "Two-Phase Flow and Evaporation in Model Fibrous Media: Application to the Gas Diffusion Layer of PEM Fuel Cells," J. Power Sources, 178(1), pp. 258-268
- [8] Or, D., Lehmann, P., Shahraeeni, E., and Shokri, N., 2013, "Advances in Soil Evaporation Physics—A Review," Vadose Zone J., 12(4), pp. 10-16.
- Shokri, N., Lehmann, P., and Or, D., 2008, "Effects of Hydrophobic Layers on
- Evaporation From Porous Media," Geophys. Res. Lett., 35(19), p. L19407. [10] Shokri, N., Sahimi, M., and Or, D., 2012, "Morphology, Propagation Dynamics and Scaling Characteristics of Drying Fronts in Porous Media," Geophys. Res. Lett., 39(9), p. L09401.
- [11] Lehmann, P., Assouline, S., and Or, D., 2008, "Characteristic Lengths Affecting Evaporative Drying of Porous Media," Phys. Rev. E, 77(5), p. 056309.
- [12] Nachshon, U., Weisbrod, N., Dragila, M. I., and Grader, A., 2011, "Combined Evaporation and Salt Precipitation in Homogeneous and Heterogeneous Porous Media," Water Resour. Res., 47(3), p. W03513.
- [13] Thiery, J., Rodts, S., Weitz, D., and Coussot, P., 2017, "Drying Regimes in Homogeneous Porous Media From Macro-to Nanoscale," Phys. Rev. Fluids, 2(7),
- [14] Shokri, N., Lehmann, P., and Or, D., 2009, "Characteristics of Evaporation From Partially Wettable Porous Media," Water Resour. Res., 45(2), p. W02415.
- [15] Chakraborty, P. P., Ross, M., Bindra, H., and Derby, M. M., 2022, "Evaporative Drying From Hydrophilic or Hydrophobic Homogeneous Porous Columns: Consequences of Wettability, Porous Structure and Hydraulic Connectivity,
- Transp. Porous Media, 143(3), pp. 551–578.
 [16] Shokri, N., and Or, D., 2011, "What Determines Drying Rates at the Onset of Diffusion Controlled Stage-2 Evaporation From Porous Media?" Water Resour. Res., 47(9), p. W09513.
- [17] Shokri, N., Lehmann, P., and Or, D., 2009, "Critical Evaluation of Enhancement Factors for Vapor Transport Through Unsaturated Porous Media," Water Resour. Res., 45(10), p. W10433.
- [18] Yiotis, A., Boudouvis, A., Stubos, A., Tsimpanogiannis, I., and Yortsos, Y., 2004, "Effect of Liquid Films on the Drying of Porous Media," AIChE J., 50(11), pp. 2721-2737.
- [19] Chen, C., Duru, P., Joseph, P., Geoffroy, S., and Prat, M., 2017, "Control of Evaporation by Geometry in Capillary Structures. From Confined Pillar Arrays in a Gap Radial Gradient to Phyllotaxy-Inspired Geometry," Sci. Rep., 7(1), p. 15110.
- [20] Chen, C., Joseph, P., Geoffroy, S., Prat, M., and Duru, P., 2018, "Evaporation With the Formation of Chains of Liquid Bridges," J. Fluid Mech., 837, pp.

- [21] Yiotis, A., Salin, D., Tajer, E., and Yortsos, Y., 2012, "Drying in Porous Media With Gravity-Stabilized Fronts: Experimental Results," Phys. Rev. E, 86(2), p. 026310.
- Yiotis, A., Salin, D., Tajer, E., and Yortsos, Y., 2012, "Analytical Solutions of Drving in Porous Media for Gravity-Stabilized Fronts," Phys. Rev. E. 85(4). p. 046308
- [23] Horri, B. A., Chong, M. N., Chen, X. D., and Wang, H., 2014, "Modelling of Solar Evaporation Assisted by Floating Light-Absorbing Porous Materials," Curr. Environ. Eng., 1(2), pp. 73-81.
- [24] Zannouni, K., El Abrach, H., Dhahri, H., and Mhimid, A., 2017, "Study of Heat and Mass Transfer of Water Evaporation in a Gypsum Board Subjected to Natural Convection," Heat Mass Transfer, 53(6), pp. 1911–1921.
- [25] Zhu, Y., Antao, D. S., Lu, Z., Somasundaram, S., Zhang, T., and Wang, E. N., 2016, "Prediction and Characterization of Dry-Out Heat Flux in Micropillar Wick Structures," Langmuir, 32(7), pp. 1920-1927.
- [26] Shokri, N., Lehmann, P., Vontobel, P., and Or, D., 2008, "Drying Front and Water Content Dynamics During Evaporation From Sand Delineated by Neutron Radiography," Water Resour. Res., 44(6), p. W06418.
- [27] Kumar, N., and Arakeri, J. H., 2019, "Experimental and Numerical Investigation of Evaporation From Line Sources of Water in Low Porosity Surfaces," J. Hydrol., 569, pp. 795-808.
- [28] Hillel, D., 2003, Introduction to Environmental Soil Physics, Elsevier, San Diego, CA.
- [29] De Vries, D., 1958, "Simultaneous Transfer of Heat and Moisture in Porous
- Media," EOS Trans. Am. Geophys. Union, 39(5), pp. 909–916.
 [30] Philip, J., and De Vries, D. D., 1957, "Moisture Movement in Porous Materials Under Temperature Gradients," EOS Trans. Am. Geophys. Union, 38(2), pp. 222-232
- [31] Prat. M., 2011, "Pore Network Models of Drving, Contact Angle, and Film Flows," Chem. Eng. Technol., 34(7), pp. 1029-1038.
- [32] Yiotis, A. G., Tsimpanogiannis, IN., Stubos, A. K., and Yortsos, Y. C., 2006, "Pore-Network Study of the Characteristic Periods in the Drying of Porous Materials," J. Colloid Interface Sci., 297(2), pp. 738-748.
- [33] Takeuchi, J., Sumii, W., Tsuji, H., and Fujihara, M., 2016, "Estimation of Permeability of Porous Media With Mixed Wettabilities Using Pore-Network Model," Geomate J., 11(24), pp. 2241-2247.
- [34] Takeuchi, J., Tsuji, H., and Fujihara, M., 2017, "Modeling of Permeability of Porous Media With Mixed Wettabilities Based On Noncircular Capillaries," Geomate J., 12(34), pp. 1-7.
- [35] Protolabs, 2022, "Material Comparison Guide," Maple Plain, MN, accessed Oct. 26, 2023, https://www.protolabs.com/media/uildjxyk/sla-watershed-xc-11122-120821.pdf
- [36] Pop, I., and Cheng, P., 1983, "The Growth of a Thermal Layer in a Porous Medium Adjacent to a Suddenly Heated Semi-Infinite Horizontal Surface," Int. J. Heat Mass Transfer, 26(10), pp. 1574–1576.
- [37] Fillet, R., Nicolas, V., Fierro, V., and Celzard, A., 2021, "Modelling Heat and Mass Transfer in Solar Evaporation Systems," Int. J. Heat Mass Transfer, 181, . 121852.
- [38] Dullien, F. A., 2012, Porous Media: Fluid Transport and Pore Structure, Academic Press, San Diego, CA.
- [39] Acrivos, A., and Chang, E., 1986, "A Model for Estimating Transport Quantities in Two-Phase Materials," Phys. Fluids, 29(1), pp. 3-4.
- [40] Park, I. S., Smith, J., and McCoy, B., 1987, "Intraparticle Diffusion Coefficients in Packed Columns: Measurement by Arrested-Flow Gas Chromatography," AIChE J., 33(7), pp. 1102–1109.